Materials Characterization 102 (2015) 47–61

Contents lists available at ScienceDirect

Materials Characterization

journal homepage: www.elsevier.com/locate/matchar

XCT analysis of the influence of melt strategies on defect population in Ti–6Al–4V components manufactured by Selective Electron Beam Melting

S. Tammas-Williams [a,b,*], H. Zhao [a,b], F. Léonard [a], F. Derguti [b], I. Todd [b], P.B. Prangnell [a]

[a] School of Materials, University of Manchester, Manchester M13 9PL, UK
[b] Department of Materials Science and Engineering, University of Sheffield, Sheffield S1 3JD, UK

ARTICLE INFO

Article history:
Received 9 October 2014
Received in revised form 23 January 2015
Accepted 10 February 2015
Available online 12 February 2015

Keywords:
Titanium
Additive Manufacture
Selective Electron Beam Melting
Pores
X-ray Computed Tomography (XCT)

ABSTRACT

Selective Electron Beam Melting (SEBM) is a promising powder bed Additive Manufacturing technique for near-net-shape manufacture of high-value titanium components. However without post-manufacture HIPing the fatigue life of SEBM parts is currently dominated by the presence of porosity. In this study, the size, volume fraction, and spatial distribution of the pores in model samples have been characterised in 3D, using X-ray Computed Tomography, and correlated to the process variables. The average volume fraction of the pores (<0.2%) was measured to be lower than that usually observed in competing processes, such as selective laser melting, but a strong relationship was found with the different beam strategies used to *contour*, and infill by *hatching*, a part section. The majority of pores were found to be small spherical gas pores, concentrated in the infill hatched region; this was attributed to the lower energy density and less focused beam used in the infill strategy allowing less opportunity for gas bubbles to escape the melt pool. Overall, increasing the energy density or focus of the beam was found to correlate strongly to a reduction in the level of gas porosity. Rarer irregular shaped pores were mostly located in the contour region and have been attributed to a lack of fusion between powder particles.

1. Introduction

Additive Manufacturing (AM) describes a family of technologies in which material is deposited and consolidated in successive layers using a focused heat source to build up a component from 2D slices [1]. AM techniques offer the capability of manufacturing more mass-efficient designs with topographically optimised geometries, directly from computer aided designs, without extensive machining. When combined with the associated shorter lead times, high material utilisation rates, and reduced tooling costs, this is an attractive proposition for low volume manufacturing in the biomedical [2,3] and aerospace [4] industries.

Selective Electron Beam Melting (SEBM) is a promising powder bed AM technique for near-net-shape manufacture of high value titanium components. The SEBM system developed by Arcam AB, who is currently the only commercial supplier, employs a rapidly scanned beam focused by electromagnetic lenses with sufficient energy to melt the precursor powder layers [5]. This system typically uses two main scanning strategies (termed *contouring* and *hatching*, respectively) to first melt the outline of each 2D section and then 'fill in' the outline by rastering the beam within the section boundary. Unlike in most other AM systems, SEBM processing takes place at an elevated temperature. A beneficial effect of this is that it results in lower residual stresses in the deposited material [4]. Furthermore, parts are built under a controlled vacuum, which reduces the level of porosity relative to laser-based powder bed techniques, allowing densities of greater than 99.8% to be achieved [6]. However, for fatigue critical designs, the presence of even a small number of residual defects is still an important consideration.

Ti–6Al–4V samples built with the Arcam SEBM process typically exhibit tensile properties comparable to those of wrought material [7–10]. In contrast, without post-manufacture treatments, such as Hot Isostatic Pressing (HIPing), the high cycle fatigue can show large scatter [4,9,11]. For example, at the same stress ratio fatigue life can exhibit a range of several orders of magnitude [11], making qualification of aerospace components challenging. In AM research on polished test samples has found that most fatigue cracks nucleate exclusively at pores, rather than at other microstructural features [4,11], while studies using unpolished samples have found cracks to initiate at stress concentrations associated with the high local surface roughness [4,9]. The presence of defects thus currently dominates high cycle fatigue life in non-HIPed AM parts. Such pores mainly originate from trapped gas, but larger defects can also arise when there is a lack of powder fusion [12–16]. However, cracks originating from pores located near a component surface are known to result in the shortest fatigue life [4,11]. Finite element modelling has also confirmed that the spatial distribution of pores is important in determining fatigue initiation [17].

* Corresponding author at: School of Materials, University of Manchester, Manchester M13 9PL, UK.
E-mail address: Samuel.tammas-wiliams@manchester.ac.uk (S. Tammas-Williams).

http://dx.doi.org/10.1016/j.matchar.2015.02.008

With AM, the elimination of the pores, without the need for additional costly process steps, such as HIPing, would clearly be beneficial to the industrialisation of this new technology for aerospace applications. Therefore, for all AM platforms there is a requirement to develop a better understanding of the relationships between the process parameters and part geometry, and the size, density, and spatial distribution of pores found within a component. Being able to determine the probability of pores appearing in critical locations, such as near surfaces, is also particularly important. Such information is essential in developing strategies for reducing the defect content.

In AM, few studies to date have been published that have quantified the residual porosity in sufficient detail to allow reliable statistical relationships to be developed with the main process variables. Standard 2D metallographic examination on polished sections has revealed that the most common pores have a circular profile [12–14,18,19] and are relatively small (<100 μm). These defects are thought to be spherical gas pores caused by bubbles becoming trapped in the melt pool during solidification. In SLM, which uses an inert gas atmosphere, some of these pores originate from shielding gas becoming trapped during densification of the powder [20]. This is less likely to occur with high vacuum processes like SEBM, but all powder based techniques are still liable to porosity if there is contamination of the powder [12].

With SEBM, using standard metallography, generally it has been assumed that the gas pores are randomly distributed [14] and little has been reported on the effect of the process variables on their location. Studies on direct metal deposition of Ti–6Al–4V have found that, although the volume fraction of gas pores in the as-supplied powder granules affected the final volume fraction of pores, other factors such as the laser power were more important [21]. While less common, in AM other defect types have also been reported that are associated with undesirable process conditions [12,14,15,18]. Such defects generally result from a lack of fusion between granules of un-melted powder and can be more damaging because of their larger size (e.g. >200 μm [12,15,18]) and high aspect ratio. Lack of fusion defects have been reported to become more common as the beam speed increases [15]. Both gas pores, and those caused by lack of fusion, have been observed in SEBM [12–16]. Recent modelling work has shown that large tunnel defects can also be produced in AM if there is insufficient energy input [22]. However, in parts produced with optimised parameters fatal fatigue cracks have been mainly reported to initiate at near-surface gas pores [4,11]. This is likely to be due to their higher frequency in the deposited material and thus greater chance of being located close to the surface, as their more rounded morphology would produce a lower stress concentration than the more irregular lack of fusion pores [23].

The objective of this study was, therefore, to address the current lack of fundamental understanding that exists of defect–process relationships in AM with the SEBM process. To achieve this end, we have made extensive use of X-ray Computed Tomography (XCT) to quantify the size, morphology, frequency, and distribution, in three dimensional space, of the pores found in titanium test samples. This has allowed statistically valid results to be obtained with far more detailed information than has been previously possible. By using XCT systems with different resolutions, it has been possible to quantify the position of the full size range of pores to the beam scanning strategies, as well as to measure the true sizes and morphologies of the pores. This has allowed valuable insight to be gained into the origin of different types of defect and their location, with respect to the build cycle in the SEBM process. The virgin powder has also been examined for evidence to support the theory [12–14,18,19] that porosity in AM can be related to gas contamination in the powder feedstock.

1.1. Energy density

The applied energy density per unit volume (E_a) is a parameter often used in selective laser melting to compare the effect of different process parameters [24,25]. It defines the local heat input per unit volume with respect to the beam speed, power and offset between melt tracks, which are varied simultaneously. Thus, this parameter is useful for comparing different samples, as well as individual locations within a build, and is given by:

$$E_a = \frac{P}{v \cdot h \cdot t} \quad \left(\mathrm{J \cdot mm^{-3}}\right) \tag{1}$$

where: P, v, h and t are the beam power (W), beam velocity ($\mathrm{mm \cdot s^{-1}}$), line offset (mm) (spacing between melt tracks) and layer thickness (mm), respectively.

It should be noted that Eq. (1) should not be viewed as the net energy input, as it neglects coupling with the work piece, but it is a useful parameter for benchmarking the relative energy input between different process settings. With SEBM using the Arcam machine, a constant voltage (60 kV) is maintained during processing so that the power (P = current × voltage) is proportional to the beam current (I) only.

2. Experimental method

The samples analysed in this study were built at the University of Sheffield in an Arcam S12 SEBM machine. The SEBM machine was configured with the most recently released version of the control software (EBM Control 3.2 Service Pack 2) [5] and standard recommended Arcam operating procedures were used throughout. The feedstock consisted of Ti–6Al–4V pre-alloyed plasma atomised powder, supplied by Arcam, with particles ranging in size between 45 and 100 μm in diameter. As would be the case in a commercially viable process, all the powder used in this study had been recycled following the procedure described by Al-Bermani et al. [7]. Before deposition, the build chamber was taken to a controlled vacuum ($<2 \times 10^{-3}$ mbar) by backfilling with helium. The first layer of powder was deposited onto a stainless steel baseplate pre-heated with the electron beam to 730 °C (the default Arcam setting). The baseplate temperature was recorded throughout each build by a thermocouple. For all samples in this study, a 210 mm square 10 mm thick baseplate was used. Prior to melting each layer, the powder was preheated and sintered by rapidly scanning the beam to maintain the target build temperature (730 °C) and to reduce charging of the powder during the higher energy-density melting stage. Standard Arcam parameters were again used for the preheating stage. This included two consecutive steps with a defocused beam, where Preheat I scanned the entire bed and Preheat 2 then pre-scans only the areas to be melted expanded by 5 mm from their section edges. In the standard build sequence this is then followed by the melting stage, which uses a more concentrated beam and employs two separate beam rastering strategies (Fig. 1a).

In the melting stage, firstly three "*contour*" passes are used to melt the outline of each 2D section slice, starting at the section edge and moving inwards. The contour strategy (from here on referred to as *contouring*) uses a technology known as *MultiBeam*, which rapidly moves the beam so as to keep several separate melt pools active at one time. As a result of the MultiBeam settings, 50 melt pools are present during the outer contour and 10 during the inner contours. In the outer contour pass each melt pool is translated more slowly and with a lower power than for the inner two (see Table 1 for details). The centre of each section is then 'filled in' by rastering the beam in a 'snaking' melt strategy known as "*hatching*" (i.e. with a forwards and backwards beam motion with a continuous path). The stage is then incremented downwards 70 μm to achieve the correct layer height, and the next layer of powder is dispensed from hoppers and spread with a rake. The hatching direction was rotated by 90° between each layer. The beam current during hatching is not directly set by the operator, instead, it is calculated by the EBM control software and varied linearly with the length of the hatch line, such that smaller melt lengths have a lower current. Once the current is decided, a "*speed function*" is used to try to preserve a constant melt pool depth by maintaining an approximately constant ratio of

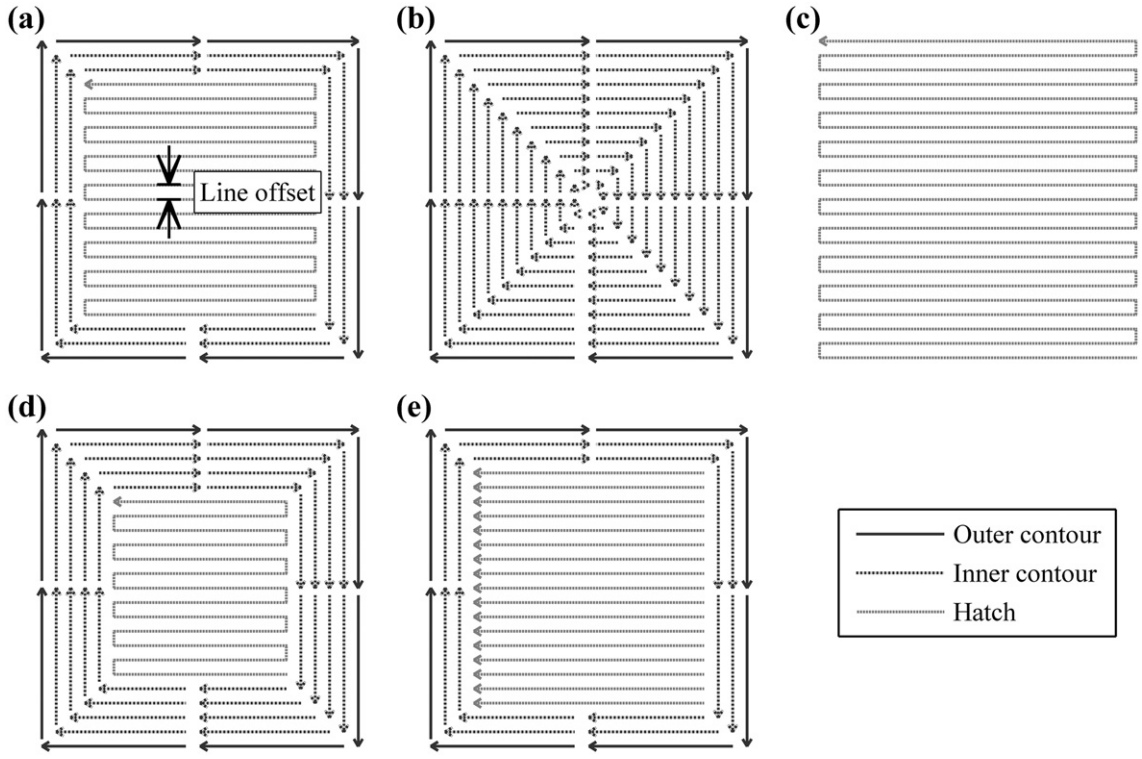

Fig. 1. Schematic diagrams of the standard melt strategy employed by the Arcam SEBM machine and those employed in the experiments conducted. (a) Default settings. First, three initial *contour* passes melt the outline of the part section, with the outer contour pass being applied first with a slower travel speed. This is then followed by *hatching* — where a single melt pool is rastered backwards and forward to fill in the outlined section. Also indicated is the direction of beam travel and line offset, which is the distance between consecutive melt track centres. (b) C1: Contour only, the number of contours is increased and each subsequent contour moved inwards until the entire cross-section is melted. (c) C2: Hatch only, no contouring is used and the hatching area is increased to cover the whole cross-section. (d) C3: Number of contour passes set to 5, giving a smaller hatched region. (e) C7: Single direction hatching, all hatch melt lines are in the same direction. Melt strategies for all other samples not mentioned were modified by changing the order in which the strategies were applied, the beam speed or the line offset between hatch passes as described in Table 2.

P/v (proportional to I/v). When the hatching reverses direction, a "*turning function*" automatically increases the beam speed, to avoid overheating the already hot recently melted area. The beam focus is also adjusted by means of a focus offset. In this case the standard procedure is to use the beam at its most focused during contouring (focus offset of 0 mA) and then defocus it slightly for hatching (focus offset of 19 mA).

To systematically examine the effect of the process parameters on the levels of porosity, simple cuboid specimens with the geometry defined in Fig. 2a, were manufactured directly onto the baseplate. The cuboids were orientated in the build chamber such that the orthogonal hatch directions (x & y) were aligned with their outer faces. During melting the samples were arranged with 30 mm between each model, to minimise thermal interaction, (significantly further than used in other studies to thermally isolate each part [13,18]). One build cycle was used to manufacture a set of specimens to examine the effect of varying the implementation of the individual contour and hatching strategies (detailed in Table 2 C0–C7 and Fig. 1b–e). Further build cycles were then conducted to systematically examine the influence of the line offset between hatch passes (L0–L2), speed function (S0–S3), and focus offset (F0–F3) during hatching, with all other parameters kept constant (see Table 2). Following each build, the beam speeds and currents used were extracted from the automatically generated log files.

Following manufacture of the test parts, the defect population in each of the samples were analysed by XCT in the Henry Moseley X-ray Imaging facility at the University of Manchester. Macro-scale scans were first performed using a Nikon Metrology 225/320 kV Custom Bay machine. These scans captured the entire cross-section of the x–y plane, but to avoid edge effects from the top and bottom surfaces, only the central 16 mm (in z) of each sample was imaged. To obtain higher resolution, small specimens were also machined from sample C0. Samples with x and y dimensions of approximately 1.75 mm were cut from

Table 1
The electron beam settings used by the Arcam machine for the different samples with the standard settings and with parameter modification (see Table 2). The corresponding applied energy density in each case E_a has been calculated by Eq. (1), based on the 'begin speed' and the average speed.

Process	Sample numbers	Melt length (mm)	v (begin) (mm·s^{-1})	I (mA)	Line offset (mm)	E_a (begin) (J·mm^{-3})	E_a (average) (J·mm^{-3})
Outer contour	All	10	280.0	5.0	0.30	51.0	51.0
Inner contour	All	9.5 & 9 (8.5 & 8 for C3 only)	700.0	12.0	0.25	58.8	58.8
Hatch	C0, C4, C5, F0, F1, F2, F3, S0, L0	9	324.3	5.7	0.20	75.5	48.4
	C2	10.6	371.7	6.1	0.20	70.8	48.4
	C3	8	294.7	5.3	0.20	77.2	47.8
	C6, C7	9	324.3	5.7	0.20	75.5	75.5
	S1	9	254.6	5.7	0.20	96.1	59.4
	S2	9	185.3	5.7	0.20	132.1	78.9
	S3	9	115.9	5.7	0.20	211.2	122.9
	L1	9	327.0	5.7	0.15	100.5	64.6
	L2	9	327.0	5.7	0.10	150.8	96.9

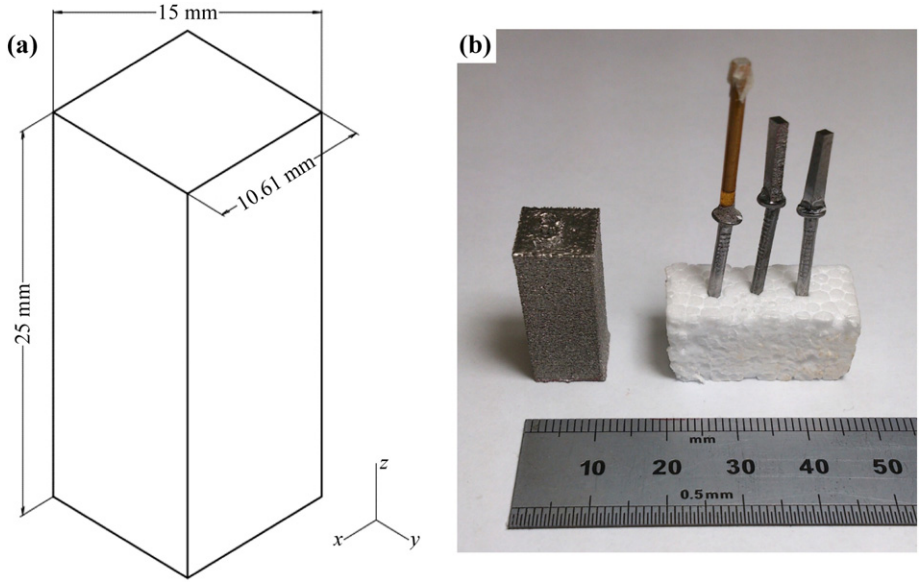

Fig. 2. The geometries of the samples manufactured and analysed by XCT; (a) the dimensions of the cuboid test samples, (b) an image showing, from left to right, examples of an as-built sample, virgin powder within a polyimide tube, and machined down microXCT specimens from the edge (HR Edge) and centre (HR Centre) of a built specimen.

both the edge (referred to as HR Edge) and centre (HR Centre). High resolution analysis of these small specimens was conducted using a Zeiss Xradia Versa 500 system, which was also used to characterise a precursor powder sample, contained in a thin walled polyimide tube. Full settings for these instruments are given in Table 3.

3D data was reconstructed from the 2D radiographs using a filtered back projection algorithm. The data was analysed using Avizo Fire 8 software with segmentation by the Otsu method [26]. Analysis was performed to characterise porosity, in terms of volume, size (the equivalent spherical diameter, defined as the diameter of a sphere of the same volume), aspect ratio (AR), orientation, and spatial distribution. The tomography data was also compared to measurements made by conventional optical microscopy from 2D sample sections in the x–y and x–z planes. Following cutting with a silicon carbide blade, the samples were metallographically prepared using silicon carbide abrasive grinding papers (P180 to P4000) before final polishing with an oxide polishing suspension. Subsequently, a Keyence confocal microscope was used to take and then stitch together 99 images of the polished unetched surfaces at 10 times magnification. The pores were quantified in MATLAB after thresholding with a value calculated by the Otsu method [26]. In addition, a qualitative analysis of the pore morphologies was carried out using back-scattered electron images, acquired with an FEI Magellan High Resolution Scanning Electron Microscope.

Table 2
Sample identification codes for all the modifications to the standard Arcam melt processes investigated, with the cuboidal shaped samples. All settings except those mentioned were kept constant at the Arcam default values.

Sample ID	Modification
C0	Standard settings (control)
C1	Contouring only
C2	Hatching only
C3	5 contours
C4	Contour inner to outer
C5	Hatch first
C6	Turning function disabled
C7	Single direction hatching
S0	Speed function 36 (control)
S1	Speed function 30
S2	Speed function 18
S3	Speed function 12
L0	Line offset 0.2 mm (control)
L1	Line offset 0.15 mm
L2	Line offset 0.1 mm
F0	Focus offset 19 (control)
F1	Focus offset 12
F2	Focus offset 6
F3	Focus offset 0

3. Results

3.1. Arcam electron beam settings

Before discussing the results, it is important to understand the effect of changing the Arcam machine process settings on the energy density delivered to each sample. When using the Arcam system it is not possible to directly alter the beam current and speed as this is calculated dynamically by the proprietary control software, based on the process settings. For all samples the contouring beam current and speed are not adjusted by the control system and did not deviate from the standard values (see Table 1). In contrast, some of the process modifications used in samples C1–C7 resulted in changes to the energy density used for hatching. At the start of each hatch melt strategy in each layer, the control system first calculates the *hatch begin* speeds, and these are shown in Table 1 alongside the corresponding beam current for the speed function. The values in Table 1 were taken from the Arcam log file, which is automatically generated during the build, and records the automatically calculated system beam parameters. It can be seen from Table 1 that there was a slight increase and decrease in both beam current and speed between the production of the standard sample, C0, and samples C2 and C3, respectively. This is caused by the change in hatch length that occurred due to the removal or addition of contour passes and occurs because the control software assigns longer hatch passes higher currents, which, through the speed function, increases the beam speed to maintain an approximately constant ratio of I/v. More significant changes in speed and energy density were recorded when the speed function was deliberately decreased in samples S1–S3.

The resultant applied energy density for each melt condition is shown in Table 1. This was calculated initially based on the 'begin speed' which suggests that hatching for the standard sample (C0) had a higher energy density than for both contours. However, although the initial hatch pass of each sample started at this speed, subsequent hatch lines are affected by a turning function, which increases their

Table 3
Instrument and settings used to acquire the XCT data.

Imaged sample size (mm)	Sample description	XCT system	Accelerating voltage (kV)	Power (W)	Exposure (ms)	Projections	Voxel size (μm)	Minimum detectable pore equiv. dia. (μm)
10 × 10 × 16	Whole samples	Custom Bay	160	17.6	1415	3143	9.9	24.6
1.75 × 1.75 × 1.75	Machined small regions	Versa 500	100	9.0	1000	1601	2.1	5.2
1.75 diameter	Powder	Versa 500	80	7.0	1000	1601	2.1	5.2

speed without increasing the beam power and thus reduces the energy density (Eq. (1)). This function is designed to increase the beam speed at the start of each new reverse hatch track to avoid overheating the already hot area recently melted in the forward pass. On turning, the speed increase is controlled by an exponential function of the initial speed and the distance from the previously melted area, while the beam power is kept constant.

The variation in beam speed and energy density with distance from the end of the previous hatch line is plotted in Fig. 3. Fig. 3 shows the values for all the hatch lines. With standard settings, the turning function can impart a maximum increase of speed of 75%, which would result in a 43% reduction in energy density at the start of the hatch pass. The effect of this speed increase can be observed in Fig. 3, by comparing samples C0 and C6, where the turning function was enabled and disabled, with all other settings kept constant. It can be seen that the turning function adjusts the speed over a considerable distance from the edge of the hatched area and in the small samples studied the speed is higher over the entire section width, never returning to its initial speed or energy density (equal to the C6 line). Thus, the actual average energy density of the hatched area is far lower than the values calculated in Table 1, based on the begin speed. The estimated actual average hatch energy has thus also been included in Table 1.

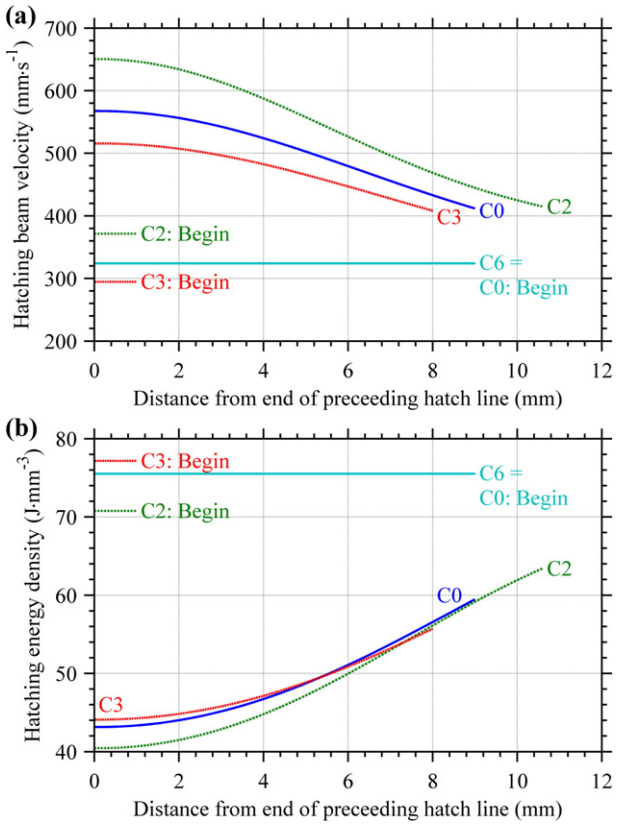

Fig. 3. The effect of the '*turning function*' on (a) the beam velocity and (b) the resultant energy density for samples (C0–C7). Note; the lines for C0 and C6 also represent the speeds of the other samples indicated in Table 1.

3.2. Overview of the XCT data from the sample built with standard conditions

In Fig. 4 isometric projections are shown of example datasets, where the segmented pore surfaces have been highlighted, that were obtained from lower resolution XCT scans performed over the whole volume of the standard sample, C0, (with a 9.9 μm voxel size) and high resolution scans carried out on 1.6 mm machined sections (with a voxel size of 2.1 μm) from the sample edge and centre (Fig. 4b). Statistical data from these scans is also summarised in Table 4. A range of pore sizes can be seen that at first sight appear randomly distributed. It should, however, be noted that because such images are projections, to the 'eye' they tend to overemphasise the volume fraction of pores. Without more careful statistical analysis such images can thus give a false impression of the density and tendency of pores to be spatially clustered. From the high resolution results, in Table 4 it can be seen that overall the volume fraction of pores measured for the SEBM process is low and in the range 0.05–0.2%. This figure can be assumed to be a lower bound because the micro-XCT system could not detect very small

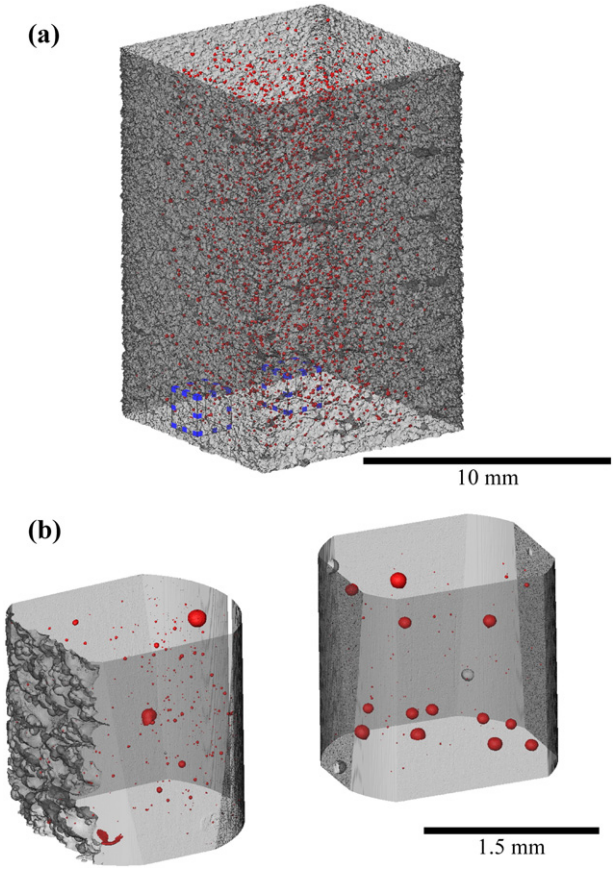

Fig. 4. Examples of XCT datasets obtained from (a) the standard cuboidal sample (C0) with a voxel size of 9.9 μm and (b) from the edge and centre of the same sample with a voxel size of 2.1 μm. The approximate location of the two high resolution scans is shown in (a) by the blue boxes.

Table 4
Summary of the average pore statistics obtained by XCT from full sample low resolution scans and from high resolution scans of different regions within the standard cube sample, C0. Also shown for comparison purposes is the data obtained by standard metallography and optical microscopy analysis of sample C0.

Technique	Sample location	Voxel size (μm)	Volume/area analysed (mm^3/mm^2)	Volume fraction (%)	Number identified	Mean equiv. diam. (μm)	Max. equiv. diam. (μm)
XCT	Whole specimen	9.9	1599.3	0.072	2707	81.7	194.6
	Hatch centre	2.1	5.3	0.176	110	19.2	139.7
	Edge	2.1	5.0	0.083	285	13.8	153.0
	Powder	2.1	2.7	0.090	970	12.1	62.6
Optical microscopy	*x–y* plane	n/a	96.8	0.126	95	21.1	159.5
	x–z plane	n/a	97.5	0.138	106	18.1	129.3

pores (less than 5 μm in diameter) and this would be expected to generate only a slight underestimate, as such pores contribute little to the overall volume.

In X-ray tomography the resolution limit is related to the voxel size and the ability to differentiate features from their absorption difference. The voxel size is controlled by the magnification (geometrical and optical) and is an absolute value determined by the equipment. For the sample sizes and instruments used in this study, the voxel dimensions are given in Table 3. The resolution is more difficult to define, but is the smallest feature perceptible from the reconstructed 3D voxel data [27]. Resolution is affected by a number of factors, including: blurring from a finite rather than point X-ray source; scatter of X-ray photons within the sample; beam hardening; mechanical errors from stage movement; and incorrect determination of the centre of rotation during reconstruction. A more thorough discussion of these effects is available elsewhere [28–30].

In the measurements performed here, the X-ray attenuation of the void within a pore was much less than that of the solid titanium background. Whilst giving good contrast, this can still be a significant issue when attempting to detect small pores in thicker cross sections. The X-ray source size always remained below the voxel size, the centre of rotation was determined to the best standard possible, and the beam hardening was reduced with a pre-filter. However, irrespective of the quality of the system setup, a single voxel can still not be quantified as it is impossible to disregard the possibility that it is simply noise in the data. In addition, to determine accurate morphological parameters like pore AR, a greater resolution is required relative to the defect size. This is because when a defect becomes too small their morphology cannot be accurately represented; i.e. ultimately a pore one voxel in size will appear as a cube. To assess pore size distributions and volume fractions a lower pore size cut-off of $2 \times 2 \times 2$ (8) voxels was therefore used and for morphological analysis only objects with a minimum volume of $5 \times 5 \times 5$ (125) voxels have been analysed, which is in line with resolution limits presented in the literature [28,30,31].

3.2.1. Pore size distributions and comparison with conventional optical microscopy

In Fig. 5 the defect size distributions obtained from the 3D datasets shown in Fig. 4, by XCT scans of the standard cubic sample (C0), are compared to conventional 2D metallographic optical microscopy measurements of the pore sizes. With the conventional optical approach, only 201 pores were analysed, despite stitching images across a total area of ~195 mm^2. In comparison, with the high resolution XCT, when two scans were added together to give approximately 10 mm^3 of material analysed, a larger number of pores was detected (395), and when the whole 1600 mm^3 sample was scanned at a lower resolution with the 225/320 kV Custom Bay machine, 2707 pores were identified.

The 3D XCT data directly provides size distributions in terms of the frequency of the equivalent spherical diameter per unit volume, whereas the optical data was measured as the equivalent circular diameter per unit area. Therefore, to allow better comparison, the optical results have been converted into an equivalent volume distribution using the Schwartz–Saltykov (S–S) analysis [32]. This analysis is only applicable to spherical objects but, as by far the majority of the pores were spherical gas pores (see below), after correction the three techniques yielded good agreement in the frequency of pores with sizes below 150 μm.

At larger sizes, insufficient pores were detected by both higher resolution XCT and optical microscopy to allow reliable statistical measurement (only 4 pores were detected with an equivalent diameter greater than 120 μm by both high resolution XCT and optical analysis). In contrast, the data from the low resolution scans in larger size ranges (>120 μm) was statistically more reliable (329 pores detected). For pore sizes smaller than 50 μm, there was also a reduction in the frequency in the macro scans, compared to the optical and the high resolution XCT measurements and macro XCT could not identify any pores below 25 μm in diameter. Thus, below the resolution limit of the macro XCT there are a large number of small pores that would be missed by this technique. There was also a small disagreement in the frequency of small pores detected between the XCT and corrected optical data. This is likely to be due to the low sample volume, as the two techniques sampled different regions of the build and there was variation in the density of porosity depending on location which will be discussed further below.

Thus, while the lower resolution XCT data cannot detect small pores, by scanning the whole sample it has identified the fewer largest pores that will be most important in terms of fatigue life which were missed by the other two techniques owing to sampling issues. The limitations in resolution and sampling statistics result in differences in measured average pore sizes. The corrected optical analysis and high resolution XCT recorded a mean size of 15 μm while the low resolution XCT gave a result of 82 μm. Overall, comparison of the three distributions shows that the majority of pores are <100 μm in diameter and few (~0.02 per mm^3) exist above 150 μm in size.

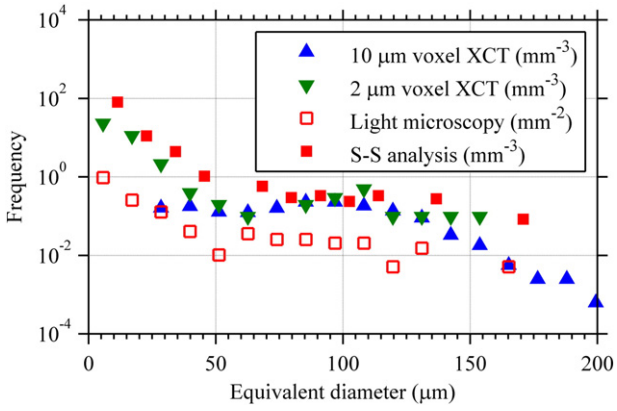

Fig. 5. Pore frequency size distributions (11.5 μm bin size) derived from XCT datasets obtained using low and high resolution scans, plotted as an equivalent spherical diameter. The XCT data is also compared to 2D data from conventional optical microscopy, using the equivalent circular diameter, as well as after conversion to an equivalent spherical diameter by the Schwartz–Saltykov method (S–S analysis) [32].

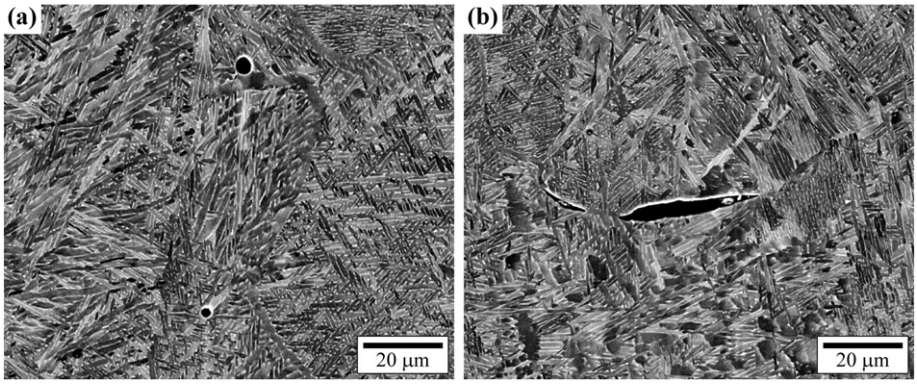

Fig. 6. Examples of typical pores seen in SEBM deposits imaged by SEM (backscatter mode) in the *x*–*z* plane; (a) two circular pores and (b) a more irregular lack of fusion pore. The build direction is vertically upwards in the plane of the page.

3.2.2. Pore morphologies

Examples of typical pores in SEBM samples when imaged by SEM are provided in Fig. 6, to enable comparison to the different pore morphologies imaged by XCT shown in Fig. 7. The pores' AR frequency distribution and their size plotted against their AR are also provided in Fig. 8, obtained from high resolution XCT scans of the centre and edge of the standard sample (C0). When observed using 2D polished sections, most pores were circular in cross section (Fig. 6a) and ranged in size between 5 and 160 μm (Fig. 5). Such pores are clearly equivalent to the very common spherical pores reconstructed from the XCT data that are designated type 'i' and 'ii' in Fig. 7. From Fig. 8 it can also be seen that all the porosity in the centre of the build (HR Centre) had a relatively low AR; the highest value recorded was 1.3. Visual inspection of the data confirms that virtually all the pores detected in the HR Centre scan were near spherical in morphology (see Fig. 4b). In addition, when the low resolution data for the entire sample was analysed it revealed that less than 3% of the pores had an AR > 1.5. A rare example of a higher aspect pore, which appears to be two spherical pores joined together, is shown as type iii in Fig. 7.

An example of a small lack of fusion defect observed rarely by SEM is shown in Fig. 6b and an irregular flaw that is equivalent to this defect is shown in 3D in Fig. 7; designated flaw type iv. Also shown in Fig. 7 is a larger rare 190 μm irregular pore (type v), observed by the macro XCT full volume scan near the edge of the sample. No corresponding SEM or optical 2D representation was found for this flaw type, because of the low frequency of its occurrence.

It can further be observed from the distributions plotted in Fig. 8 that there was a greater frequency of small high aspect-ratio pores near the edge of the sample (HR Edge). In contrast, within the hatched region the centre of the sample (HR Centre) contained few high AR pores, but a number of larger near spherical pores. However, the majority of pores identified in both samples were spherical and relatively small (<75 μm).

3.2.3. Pore alignment

In Fig. 9 the dataset from the standard sample (C0) has been used to plot histograms depicting the orientation distributions of the major axis of elongated pores, relative to the build direction (z) and the beam raster directions (x & y). It can be seen from the graphs in Fig. 9 that the pores were found to have their largest axis strongly orientated close to the x–y plane, whereas the rotation angle around the build direction showed no preferential alignment with the orthogonal scanning pattern. Hence, irregular pores were found to be elongated in the plane of the deposited layers but were not strongly orientated relative to the beam raster directions.

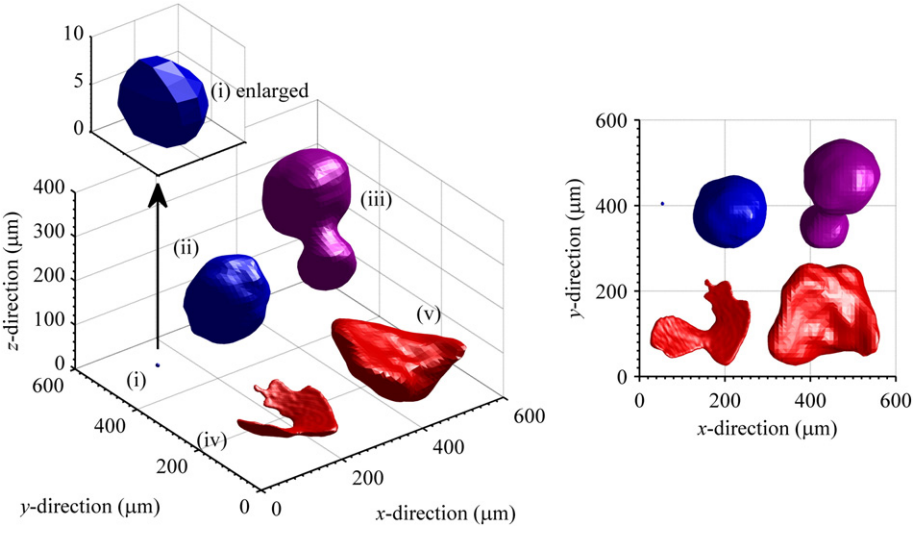

Fig. 7. Examples of pore types observed in the AM builds from the standard sample, C0, at the same scale and translated to fit on a single figure: spherical pores, small (i) and large (ii) (blue); (iii) two near spherical pores joined together (turquoise); irregular pores, small (iv) and large (v) irregular (red). The build direction is *z* while *x* and *y* denote the *hatching* directions. An enlarged view of the small type '(i)' pore is provided in the inset. Note; of the smaller/thinner pores (types i & iv) were detected using a high resolution scan from the centre of the sample and the coarse pores (ii, iii & v) were imaged using a lower resolution full sample scan. The very small spherical pore (i) has also been enlarged in the inset.

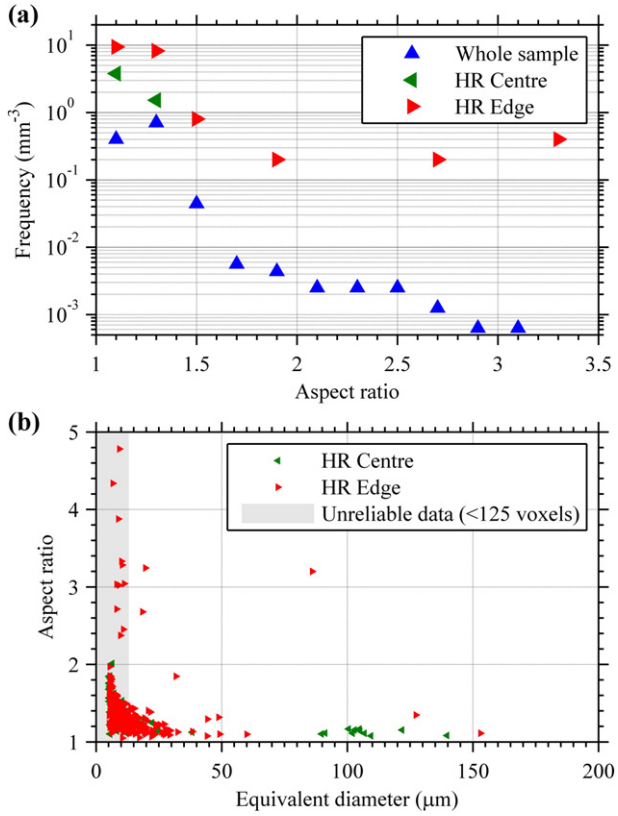

Fig. 8. Pore aspect ratios obtained from the standard sample (C0) from high resolution data XCT taken at the sample edge and centre and lower resolution data from the whole sample, plotted as; (a) ratio frequency distributions and (b) AR against equivalent diameter distributions for all the pores, including those too small to allow reliable AR calculations (i.e. less than 125 voxels in size). Note the increased frequency of irregular pores in the sample taken from the cube edge.

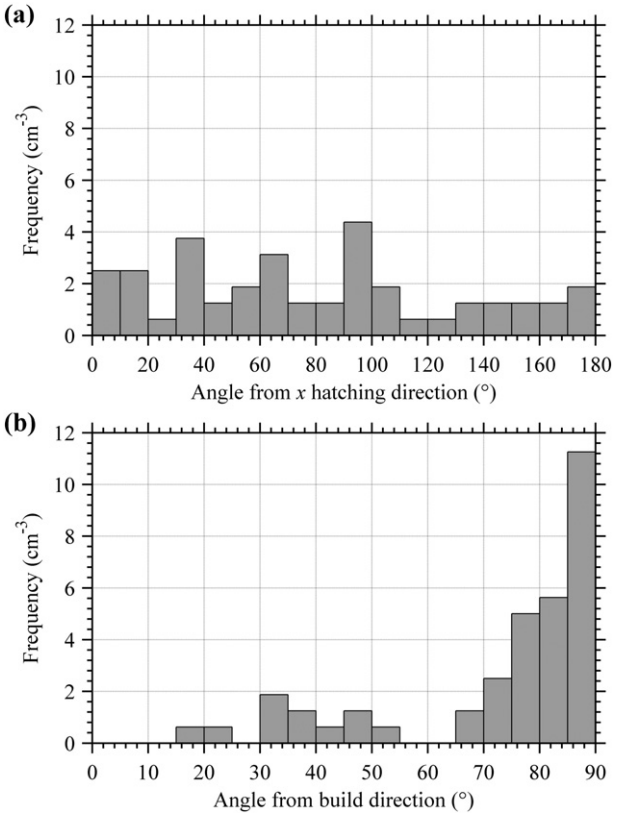

Fig. 9. Orientation distributions of irregular pores determined from (a) the angle of their major axis to the build direction and (b) the rotation of their major axis around the build direction in the *x*–*y* plane, relative to one of the *hatching* raster directions (lower resolution dataset from the standard cuboidal sample C0).

3.3. Measurements from the powder feedstock

Statistical results from XCT scans of the powder feedstock are depicted in Fig. 10. The measured size distribution of the powder particles was 45 to 100 μm range, with only 8% of the particles falling outside this range. From Fig. 10, it can be seen that a significant fraction of the larger powder particles contained pores. 6.4% of the particles over 40 μm in size had internal pores, whereas none were detected in particles smaller than this size. The pores present within the powder particles have also been compared to those in the consolidated material in Table 4. From these measurements it can be noted that the volume fraction in the powder was lower by a factor of ~1.5–2, relative to that in the centre of the standard AM sample (HR Centre), while the number density (pores per unit solid volume) was an order of magnitude higher within the powder feedstock.

3.4. Effect of the different melting strategies

As has been noted above, the pores in the sample centre which came from the hatching region tended to be more spherical, with irregular pores occurring predominantly near the sample edge. The size, shape, and spatial distribution of the pores, relative to the process strategy, are considered further below.

3.4.1. Spatial distribution of pores in the x–y plane

The macro-XCT 3D pore datasets for the standard samples have been compressed in the build direction in Fig. 11, to allow visualisation of the spatial distribution of all the coarse (>25 μm) pores found with proximity to the sample edges. The pore volume fractions have also been averaged with distance from the sample surfaces to the centre of each section and these results are plotted in Fig. 11a. Fig. 11c and e also shows the relative volume fractions of regular (AR ≤ 1.5) and irregular porosity (AR > 1.5). Since it was only possible to measure the AR of pores greater than 125 voxels in size, the volume fraction of these pores is also shown for comparison in Fig. 11. From Fig. 11a, it is clear that larger pores (>125 voxels) make up the majority of the measured volume fraction. It is also apparent from Fig. 11 that the standard specimen had a low volume fraction of pores near its edge, within a distance consistent with where the powder was melted by the contouring passes, whereas in the middle hatching region the average pore density was substantially higher. Moving inwards, two peaks in porosity are also observed in the data in Fig. 11a. The first smaller peak (denoted I in Fig. 11a) is at a distance of ~0.8 mm from the section surface, which coincides with a position close to the location of the last contour pass and the edge of the hatching region (shown by the light line in Fig. 11). However, there is a much larger second peak (II) in pore volume fraction between ~1.5 and 2 mm from the surface (in the x–y plane), near the edge of the hatching region. From Fig. 11c and d it is clear that both peaks are almost entirely due to an increase in volume fraction of porosity with a spherical morphology. It is also notable that moving in from the surface, in the initial 0.7 mm the porosity is almost entirely irregular (Fig. 11e and f). Whereas further from the surface irregular porosity only makes up a small fraction of the total pore volume fraction.

3.4.2. Effect of process modification

To aid visualisation of the pore densities, in Fig. 12 all the pores detected in the macro-scale XCT scans of samples C0–C7 that were produced with different process modifications have again been projected into the x–y plane. In Fig. 13 the total pore volume fractions have also

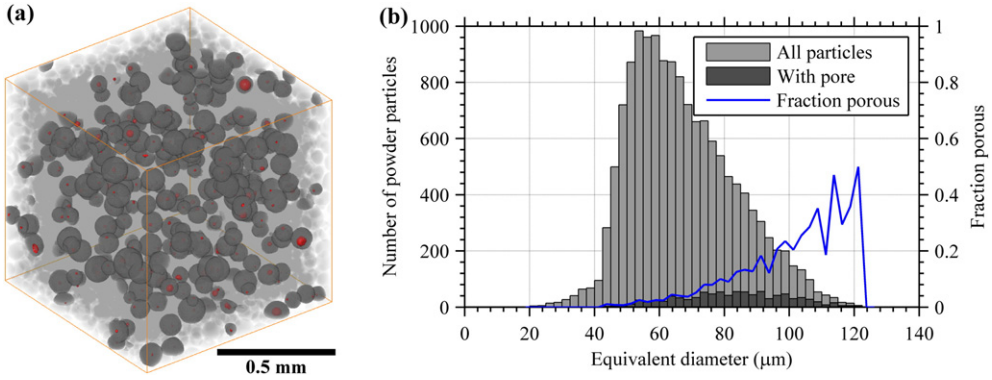

Fig. 10. (a) XCT image showing example powder particles containing gas pores and (b) size distributions of all the particles and only the particles containing porosity. Also indicated in (b) is the fraction of particles found to contain pores for each size bin.

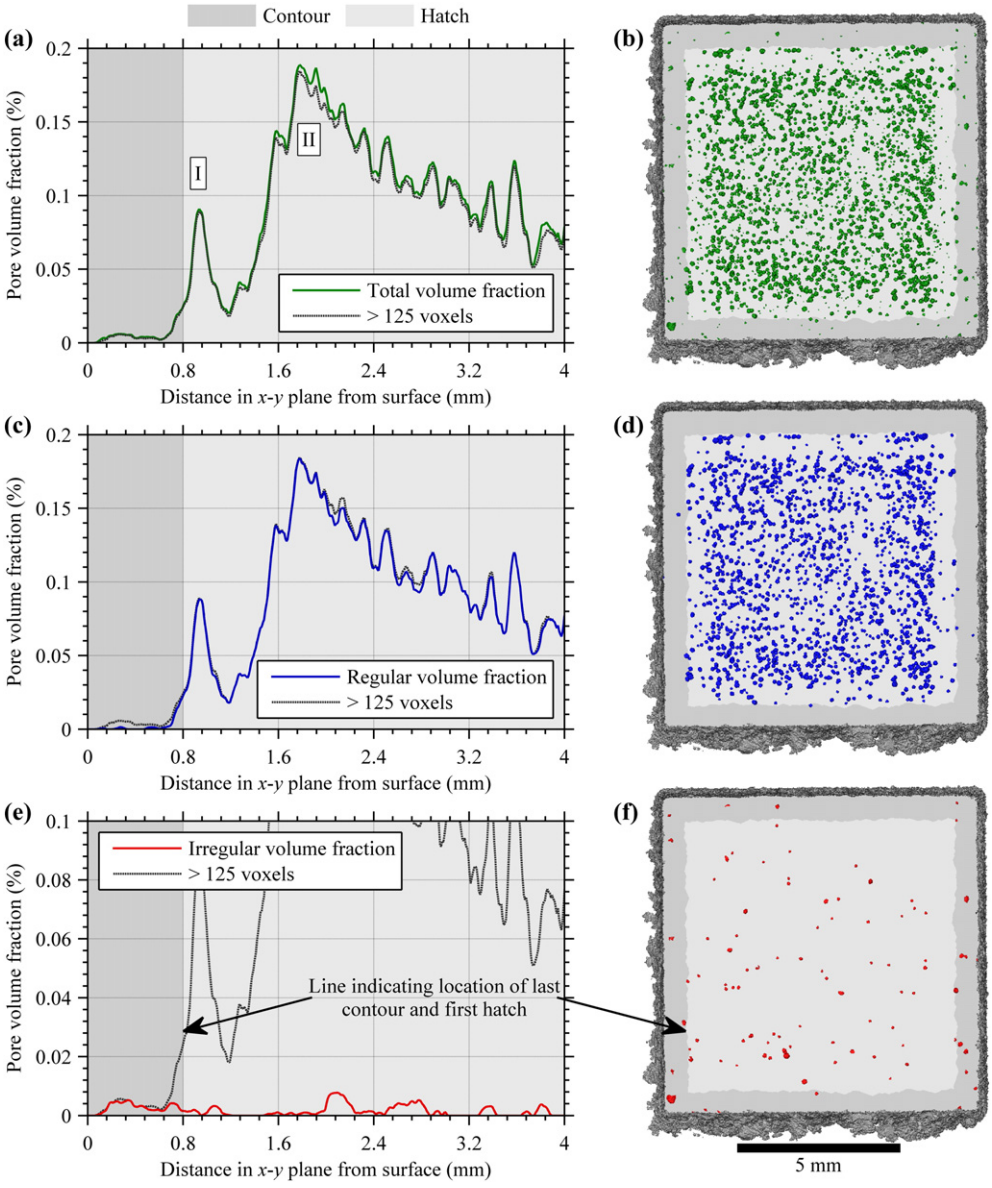

Fig. 11. Lower resolution analysis of the standard sample C0 showing the variation in porosity volume fraction in the *x–y* plane with distance from the sample surface; (a) the variation in the total pore volume fraction; in (b) all the pores detected are also projected in to the *x–y* plane, to allow visualisation of their spatial distribution; in (c) and (d) quantification and visualisation of only the regular pores is shown, (e) and (f) provides data for the irregular pores. In all images the approximate width of the regions melted by contouring and hatching are denoted by the background colour. On all images the line at 0.8 mm from the surface indicates the location of the last *contour* pass. The volume fraction of pores large enough (>125 voxels) to allow accurate shape measurements is also indicated.

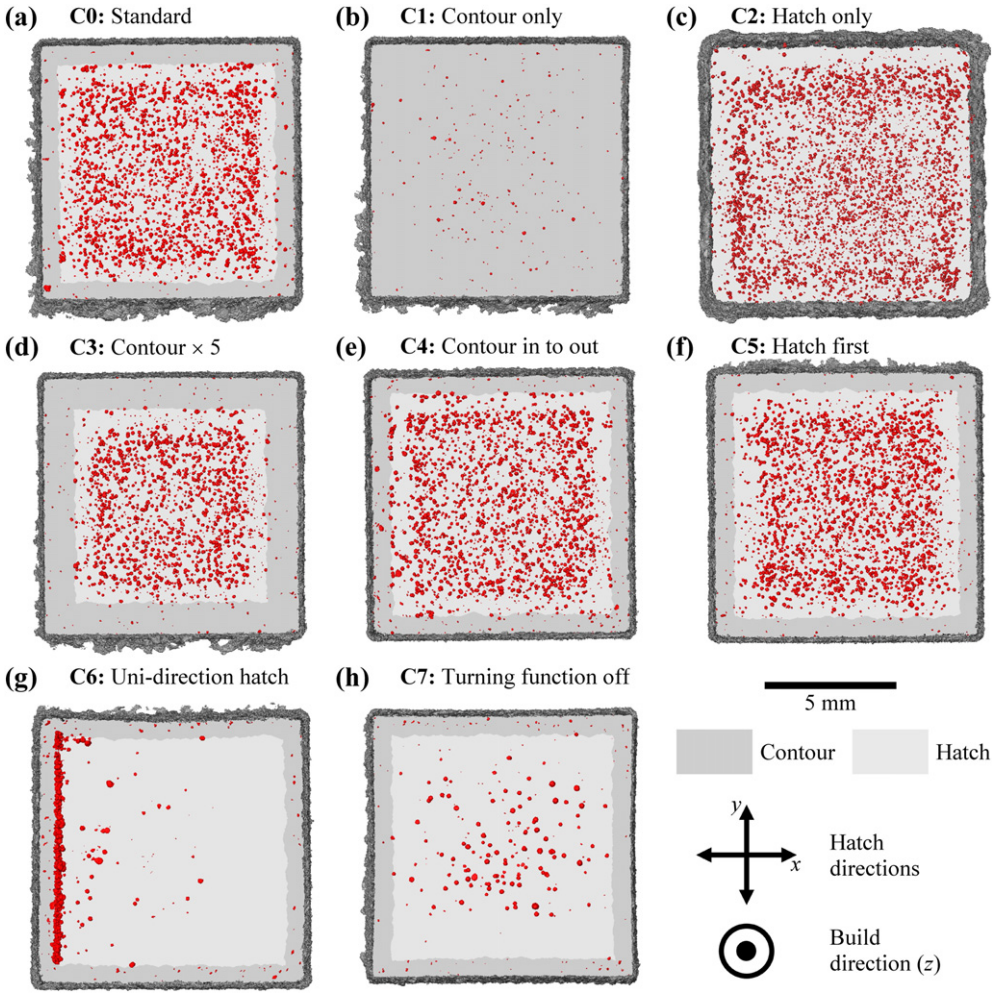

Fig. 12. Lower resolution 3D XCT full sample scans showing all the pores (red) detected in each sample projected in to the *x*–*y* plane to allow visualisation of their spatial distribution, showing (a)–(h) the effect of the process modifications defined in Table 2. In all images the approximate width of the regions melted by contouring and hatching are denoted by the background colour.

again been plotted with distance from the sample surfaces and the overall volume fractions of the porosity in all the samples are indicated in each legend. It is immediately obvious from comparing the images in Fig. 12 and the graphs in Fig. 13, that changing the machine settings can radically affect the distribution and density of pores. For example, build C1 (Fig. 12b), produced by only using the contour settings across the entire section, had an average pore volume fraction much lower than that seen for the standard build. In addition, this build did not show any strong peaks in void density (Fig. 13a). In contrast, sample C2, (Fig. 12c) which was produced by hatching across the entire section, had a higher pore density than the original standard sample and a peak in pore volume fraction at a distance of 1.1–1.3 mm from its edge, similar to the second peak (II) seen in the standard build (Fig. 11). It is notable that this peak had moved outwards by the same distance (0.8 mm) as the extra hatching length required when contouring was turned off. This larger peak must therefore be a feature of only hatching and not due to the interaction between the hatching and contouring regions.

Furthermore, when the number of contour passes was increased from 3 to 5 (sample C3) the surface layer with low porosity became correspondingly wider and the first smaller peak in pore density (I in the standard sample) moved inwards by a distance equivalent to that of the offset caused by the additional two contour passes (2 × 0.25 mm) to 1.3–1.4 mm (Fig. 13b). In addition, when contouring was changed so that the first contour pass started at 0.8 mm in from the surface, and the subsequent passes moved out to the edge of the specimen (sample C4, Fig. 12e), the variation in volume fraction with depth was very similar to that recorded with standard settings. However, when the contouring was performed after the hatching, (sample C5,) the first peak (I) was no longer observable, but the larger second peak (II) was again present in the same location as in the standard build (Fig. 13c). In contrast, when the snake function was turned off (sample C6) so that the hatching was performed by sweeping in a single direction, (right to left in Fig. 12g) the first peak became far more pronounced, while the second peak disappeared. From Fig. 12g (sample C6) it also appears that there is a tendency for pores to be left closer to the end (left) of a hatch track than the start (right). Therefore, it can be concluded that peak I is probably generated by the end of the hatching lines.

Single direction hatching would also negate the effect of the turning function as the beam would not turn back on itself and as a result there is no peak II in the hatching region. To confirm this relationship in sample C7 (Fig. 12h) normal hatching was resumed, but the turning function was disabled and the overall density of pores can again be seen to be much lower in the hatching region than in the standard sample.

3.4.3. Influence of beam speed, offset and focus on pore volume fractions

Finally, Fig. 14 summarises the effect of changes to the beam speed, hatch offset, and focus on the measured pore volume fractions obtained by the lower resolution XCT full sample scans. For these experiments, all the other beam parameters were kept constant (see Table 2). It is clear from Fig. 14 that decreasing both the beam speed and hatch offset

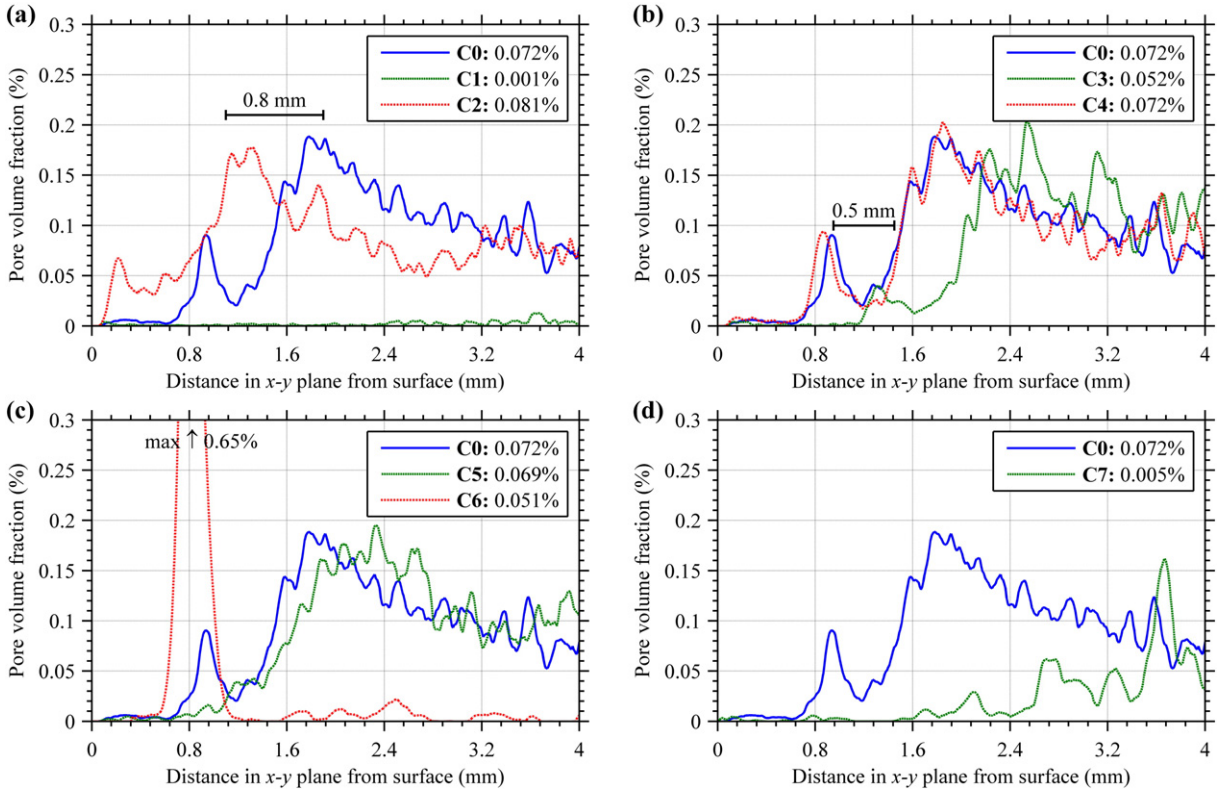

Fig. 13. Effect of process modification, compared to the standard recommended settings (sample C0), on the pore volume fraction distribution with distance from the build edge, from lower resolution XCT scan data. The parameters changed are described in Table 2 for each sample type (C1–C7). The average volume fraction for the whole sample is given in the figure legend.

reduces the level of porosity (>25 μm diameter). However, the relationship between focus offset and pore volume fraction was found to be more complex. A reduction in focus offset, from its standard value (F0: Focus offset = 19 mA) first reduced the detected pore volume fraction by an order of magnitude, before increasing it slightly again when the beam was at its most focused (F4: Focus offset = 0 mA).

4. Discussion

The systematic approach outlined above has made use of 3D XCT datasets to quantify the type, size, and spatial distribution of the residual pores found in the SEBM-AM test samples in more detail than has previously been reported. This analysis was first performed at the scale of the whole sample, with a bigger voxel size, to determine the location of larger (>25 μm) defects. Subsequently analysis was performed at a finer scale in specific regions of selected samples, with an order of magnitude smaller voxel size, under conditions that were capable of detecting nearly all the pores present, down to a size limit of ~5 μm in diameter. The results have revealed that, although the average volume fraction is quite low (<0.2%), the pores present are not randomly distributed; rather there is strong evidence of a link between the pore distributions, beam scanning strategies, and beam control parameters. These factors are discussed in turn below.

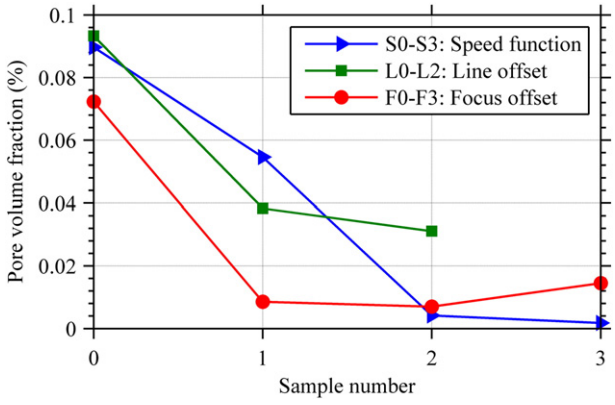

Fig. 14. Influence of the speed function, line offset and focus offset on detectable pore (>25 μm diameter) volume fraction. The sample codes are described in Table 2.

4.1. Pore formation

The present study has confirmed previous observations that small spherical pores less than 100 μm in diameter, such as those depicted in Figs. 6a and 7 (types (i), (ii)), are by far the most common defect found in SEBM-AM components (97% of the total) [12–14,19]. Their smooth spherical morphology confirms their origin as gas bubbles that were unable to escape during solidification [12]. Because the SEBM processing is carried out under vacuum, the main source of gas pores is thought to be argon from the powder feedstock that has been trapped in the powder particles during their manufacture by plasma atomisation. Clear evidence of this source of gas contamination has been found by scanning the virgin powder, which has revealed a significant level of pores within larger powder particles (Fig. 10). The volume fraction of pores measured in the powder was 0.09% compared to 0.18% in the consolidated material, but the average number density of pores was lower by 90% in the solid samples (Table 4). The average size of the argon bubbles in the precursor powder granules was 12 μm. Although the maximum pore size in the powder must be less than the maximum size of the particles (~100 μm), gas bubbles can potentially expand in the melt pool as the gravitational hydrostatic pressure from the small melt pool would be low and there was a reduced pressure of 2×10^{-3} mbar in the build chamber. Gas bubbles swept forward by

the solidification front could also coalesce. An example of two gas pores frozen in the process of coalescing is shown in Fig. 7 (type (iii)). The lower volume fraction, but higher number density, of argon filled pores in the powder can thus easily account for the observed level of gas porosity seen in the consolidated samples and implies that a substantial proportion of this gas is actually lost from the melt. Bubbles formed by soluble gases, such as H_2, O_2, and N_2 can also potentially precipitate at the solidification front, due to the large difference in their solubility in the solid and liquid phases [33]. However, to be a significant source of porosity, this would require a higher level of contamination than has been measured in the materials used in this study; measured gas concentrations were only H: 0.0015 wt.%, N: 0.015 wt.% & O: 0.121 wt.% [34].

Whether or not a gas bubble can escape before becoming trapped during solidification, by breaking the surface of a moving melt pool, depends on the pool shape as well as the convective and buoyancy forces that control their motion [35]. The high beam travel speed in AM processes typically results in a tear drop shape that is relatively shallow, but very elongated [7,36]. This melt pool shape would make gas escape easier than, for example, in laser welding where the pool is typically much deeper. However, the high speed of beam travel and related rapid solidification rate in AM is generally believed to increase the probability of gas entrapment [12].

The presence of irregular shaped pores in AM builds is potentially more damaging owing to the higher stress concentrations they can generate. Such pores were found to form a minor fraction of the population with only ~3% of pores having an AR > 1.5 in macro-scans of the standard sample. Higher resolution scans revealed no pores with AR > 1.5 in the centre of the hatched region (HR Centre) but 4.2% by number were found at the edge of the sample (HR Edge). These irregular defects had a wide size range, from a minimum of 18 μm up to 190 μm (Fig. 8b). The smaller irregular pores (type (iv) in Fig. 7) had a morphology that suggests that they were formed from a lack of fusion and arise from small voids left between partially melted powder particles. It has been demonstrated that the irregular pores showed a strong tendency to be orientated with their major axis (Fig. 9) lying in the plane of each layer, but that they were not found to have preferential alignment with the orthogonal beam raster directions. This in-plane alignment is to be expected if the irregular pores arise from gaps between partially melted powder particles, owing to the semi-circular transverse section of the melt pool and gravity driven compaction of the semi-solid region during processing.

Irregular pores could be generated by random intermittent irregularities in the process, which reduces overlap of the melt tracks (e.g. where there has been poor local powder settling during spreading) or there was a particularly coarse particle near the edge of the melt pool, or as a result of local variation in coupling of the moving beam and the material in the powder bed. However, although they were found throughout the samples, they were dominant in the contour region where, entirely opposite to in the hatching region, they made up the majority of the detected defects. A possible reason for this is the Arcam MultiBeam setting, which keeps 10 melt pools active during contouring. This could lead to a non-steady state response with more chance of material intermittently not fully melting. Contouring also employs a more focused beam than the hatching, which Al-Bermani [37] showed results in a deeper but narrow melt pool, and this could potentially lead to insufficient overlap between passes, although the discussion below will show that beam focusing is generally beneficial to achieving higher levels of densification.

4.2. Influence of energy density

To better understand the differences between the samples, the overall approximate average energy density used to melt each of their cross sections has been calculated by integrating the beam velocity over the entire hatch length (i.e. including the effect of the turning function) and summing the proportions from the contouring and hatching regions relative to their respective area fractions. Fig. 15 shows the calculated average energy density plotted against the observed volume fraction of porosity for the individual changes to the process (C0 to C7) as well as the effect of more systematic changes to the *speed function* and *hatch* offset. From Fig. 15 it appears that the energy density and porosity volume fraction have an inverse relationship. Therefore, it seems likely that as an increased energy density results in larger and deeper melt pools, with greater overlap and re-melting in repeated passes, this gives more opportunity for gas bubbles to escape.

Although the energy density provides a convenient way for broadly comparing the effect of line offset and beam speed, it appears, from the scatter in Fig. 15, that other individual factors can be more important. For example, lowering the beam speed (samples S0 to S2), which will increase both the melt pool width and depth, appears to be more beneficial than reducing the overlap (samples L0 to L2). In addition, it appears that a lower focus offset has a very substantial effect on the measured volume fraction (samples F1, F2 and F3). The beneficial effect of focus and other aspects of the beam control, such as the turning function, are discussed further below.

Unfortunately, there is currently little published data from SEBM-AM samples with which we can corroborate these observations. With similar laser based (e.g. SLM) processes, results reported on the effect of energy density on residual porosity levels are very scattered, as individual variables such as speed can have separate effects on melt pool stability. Hence, higher energy densities do not always result in more dense parts [24,25,38–40]. Previous SEBM work has shown that when the beam speed or hatch offset is reduced, which would increase the energy density, the volume fraction of lack of fusion defects can be reduced [15,39]. The presence of very large tunnel defects (none of which were observed in the work presented here) has equally been predicted to be caused by an insufficient energy input [22]. However, the results here suggest that the volume fraction of gas pores, as well that of lack of fusion defects, is reduced when the energy density of the electron beam is increased above the Arcam recommended standard settings. In direct laser melting of stainless steel powders, increasing the energy input to aid removal of gas pores has equally been shown to lead to lower porosity, in that work it was suggested that remelting of previously solidified layers without more material deposition was effective in helping gas bubbles to escape [20]. Increasing energy density is not without drawbacks; in addition to elevated operating costs, it is associated with an increased level of aluminium evaporation [41], which may alter both the microstructure and mechanical properties of components.

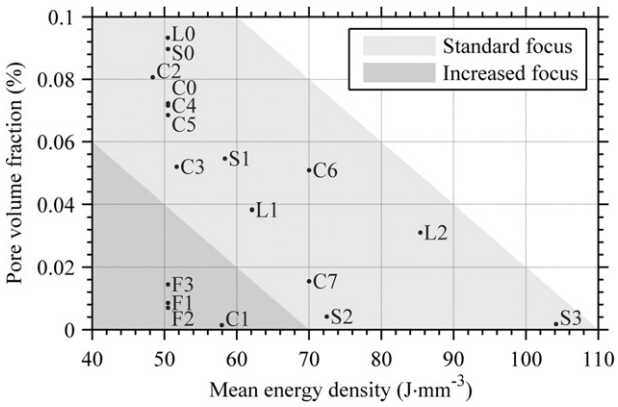

Fig. 15. Sample average pore volume fractions, measured by low resolution XCT, plotted against the average energy density for a whole layer in each sample, produced with different process parameters (see Tables 1 & 3). The background colour indicates whether the focus offset was different to the standard focus offset used during hatching for the majority of the build.

4.3. Effect of the different melt strategies

The observed trends in porosity density as a function of distance from the surface measured in the samples (Figs. 11 to 13) suggest that the pore distribution is influenced, in particular, by differences between the contouring and hatching beam parameters. A substantially lower average porosity was repeatedly found in the contouring region than in the hatching area, which had a far larger pore volume fraction (Table 4), although in the hatch region they were mainly spherical gas pores (Fig. 8). Thus it is apparent that the smaller melt pool, higher beam speed, and reduced overlap between layers associated with the hatching have given less opportunity for any gas bubbles to escape.

A further important observation is that the pores were not uniformly distributed across the standard sample section, even if the beneficial effect of the contour passes was not considered. Peaks in porosity were repeatedly found at two specific locations; at the absolute edge of the hatching area and further inwards where the pore volume fraction rises towards the edge of the hatch region. These peaks have been identified as I and II in Figs. 11 and 13. In the sample sections built with standard parameters, a smaller narrow peak (I) in pore volume fraction was seen at ~0.9 mm from the edge, where relatively large spherical pores dominated (Fig. 11). In contrast the larger peak (II) builds up sharply at depth of 1.6 mm before decaying towards the build centre to the higher level seen in the hatched region. A similar trend for pores to be located near the edge of the hatch region was observed in metallographic images of non-optimised builds by Karlsson et al. [14]. In the work here these two positions of pore concentration have been shown to be clearly related to the edge of the hatching lines. For example, when a sample was produced just by using contouring, which spiralled inwards from the edge, very few pores and no peaks in the pore population were found. In addition, when the hatching strategy was changed to rastering in one direction only, pores were found at the end of the hatching lines at the position of peak I. This implies that pores pushed forward by the solidification front tend to be dumped at the end of the hatching track and it is likely that this also happens when the beam abruptly reverses direction when the normal weaving raster pattern is used. Whatever the origin of these pores, it is apparent that they were removed by re-melting the edge of the hatching area, when contouring was performed after hatching (sample C5, Fig. 13c).

Hence, although the higher heat input and larger overlap of the contour melt tracks tended to reduce gas porosity in general, by allowing more opportunity for gas bubbles to escape from the larger melt pool, there also appears to be a negative effect of a sudden change of beam direction associated with hatching, which does not happen in contouring.

The presence of peak II within the hatching area can be explained by considering the effect of the turning function which increases the beam speed, reducing both the energy density and the time available for gas bubbles to escape towards the start of each raster line (see Fig. 3). A moving melt pool will also become narrower and less deep, in response to a higher travel speed, thereby reducing the melt track overlap, if this is not adequately compensated for by residual heat from the previous pass. In fact, the rise in porosity towards the edge of the hatching region shown in Fig. 11a mirrors the change in energy density plotted in Fig. 3b. Hence, the turning function appears to increase the probability of gas pores remaining trapped in the melt pool close to the edge of the hatching area. This implies that the energy input near the edge of the hatch region is reduced too far by this control function, and there is not sufficient re–melt depth to give gas adequate opportunity to escape from the melt pool. This conclusion has been confirmed by the observation that the peak in porosity near the edge of the hatched area disappeared when the turning function was disabled (Figs. 12h, 13d) which would increase the energy density at the edge of the hatching area.

In addition, in the sample produced when hatching with a constant beam speed (C7), the overall volume fraction of porosity was lower across the entire section and an inverse behaviour was found, in that the pore density decreased towards the edge of the sample (Figs. 12h, 13d). This occurs because when the turning function is disabled, the melt tacks will actually become wider and deeper near the edge of the hatch region than the centre, because of the residual heat from the forward beam travel.

Although powder bed AM is most suited to producing complex, relatively small components, it should also be noted that when melting parts with thicker sections, the turning function will have a smaller effect. As the average energy density will be higher it is likely that the number of pores will be lower than in the samples examined here.

The trough in pore volume fraction between peaks I and II is not as easily explainable without more information concerning the transient melt pool behaviour as the beam path reverses direction through a tight arc as it moves to the next hatch line (Fig. 1). This relatively low porosity region was still observed when only hatching was used to melt the sample (C2, Fig. 13a), at approximately 0.5 mm from the hatch region edge. When the electron beam reverses direction it will first have to accelerate to the high speed requested by the turning function. This region, which is close to the turning point, therefore, probably does benefit from the additional residual heat from the previous track. In addition, if gas bubbles that build up by being at the rear melt pool surface in the forward motion of the prior beam track are dumped out during turning, there will be a brief period before the number of bubbles build up again to a steady state level.

It is notable that the porosity recorded within the contour only sample (C1) was significantly lower than for hatched sample S1 which was produced with the same energy density via modifications to the speed function. This could be related to the lack of beam turning in the contour patterns, but with samples F0–F3 it has been shown that this could also be due to the more focused beam used by the Arcam machine, when contouring is used rather than hatching. The reduction in pore volume factions in samples F0–F3 suggests that when the focus of the beam is increased the probability of gas bubbles escaping the melt dramatically rises. Al-Bermani [37] has shown that in the SEBM process, the focus offset had a significant effect on the melt pool geometry. In particular, a lower focus offset (closer to 0 mA) was found to result in a narrower but deeper melt pool. Thus, increasing the amount of remelting of the previous layer seems to be an important factor in reducing the level of porosity. This could also be the main benefit from increasing the energy density by reducing the travel speed in the results described above. Indeed, in Al-Bermani's work, the deepest melt pool was measured with a focus offset of 10 mA that produced a focal point just above the surface [37]. This would imply that samples F1 and F2 would have also have had greater melt pool depths, which could assist in the escape of gas bubbles, by a greater level of re-melting of the previously consolidated layer.

5. Conclusions

The, size, volume fraction and spatial distribution of pores found in the SEBM-AM test samples have been characterised in more detail than previously been reported, using 3D XCT datasets. The strong trends in the results reported are partly symptomatic of the fact that similar 3D data, to that presented here, has not been previously widely available to aid equipment manufactures in optimising their control algorithms specifically for porosity reduction. However, it should be remembered that the machine default process settings in AM are designed not just to optimise porosity, but also through consideration of other competing factors, such as the part build rate and microstructure. In addition it has been shown that significant improvements can be made by relatively simple adjustments to the standard equipment settings.

Overall, the results from high resolution XCT scans gave good agreement with more conventional 2D measurements by optical microscopy, down to a size limit of ~5 μm in diameter, giving confidence in the results. However, coarser scale scans with a resolution limit of ~25 μm were found to be very useful for locating all the larger scale flaws within an entire build. Encouragingly, analysis of the XCT data has shown that

the average volume fraction of the pores was very low (<0.2%) and bellow that usually found in other AM processes like SLM (e.g. [24,38,39]).

The pores/defects have been conclusively shown not to be randomly distributed, and a strong correlation was found with the process parameters and strategies used to outline (contouring) and infill (hatching) a part section, making their impact on fatigue life potentially more significant. With the standard build parameters, it has been found that the vast majority of voids were small spherical gas pores. These pores are thought to predominately originate from argon contamination in the powder feedstock, with the smaller gas bubbles trapped in the powder granules expanding and coalescing in the melt pool, owing to the reduced pressure in the build chamber. Rarer irregular shaped pores were found to be related to a lack of fusion between layers. Some of these flaws were quite large (up to 190 μm) and they were predominantly concentrated in the contour region.

Few gas pores were found within the surface layer melted by the contour passes, with the majority being concentrated in the infill hatched area. This behaviour has been attributed to the higher energy density used in the contour step. This produces a larger, and more importantly deeper melt pool, giving more opportunity for gas bubbles to escape by encouraging a greater level of re-melting of the previous layer. The irregular shaped pores found within the contour region are assumed to be an artefact of the MultiBeam setting not giving sufficient melt pool stability, but more work is needed to definitively prove this connection. Overall, the lower average energy density in the hatching region clearly correlated to a higher average gas pore density. Simple changes to the process parameters to increase the energy density in this region produced significant reductions in the pore populations. In addition, the use of a more focused beam offered the opportunity to reduce the gas porosity without increasing the energy input, owing to the deeper melt pool this generates.

Under standard build conditions, moving in from a section edge, two peaks in porosity were seen at depths of 0.9 mm and 1.6–2 mm. Both peaks were related to the edge of the hatching region. The first peak was formed by gas bubbles being moved to the edge of each hatch pass and subsequently deposited at the end of a hatch line, when the melt pool changes direction. The second peak is thought to be due to the effect of the turning function within the hatching region. It appears that this function overcompensates for residual heat left by the forward beam pass, by overaccelerating the beam when it reverses its trajectory. This results in too low energy density, which leads to more gas pores being seen near the edge of the hatched area.

Acknowledgements

The authors acknowledge funding from EPSRC for the Henry Moseley X-ray Imaging Facility under EP/F007906/1 and EP/F028431/1, the Advanced Metallic Systems CDT (EP/L016273/1) at the Universities of Manchester and Sheffield and LATEST2 program (EP/G022402/1). (For access to the original data used within this article, please contact the corresponding author.) Thanks also go to Everth Hernandez Nava, Jack Donoghue and Jefri Draup, for their assistance in the production of this paper.

References

[1] I. Gibson, D.W. Rosen, B. Stucker, Additive Manufacturing Technologies, 1st ed. Springer, London, 2010.
[2] G.P. Dinda, L. Song, J. Mazumder, Fabrication of Ti–6Al–4V Scaffolds By Direct Metal Deposition, Metall. Mater. Trans. A 39A (2008) 2914–2922.
[3] P. Heinl, L. Müller, C. Körner, R.F. Singer, F.A. Müller, Cellular Ti–6Al–4V structures with interconnected macro porosity for bone implants fabricated by selective electron beam melting, Acta Biomater. 4 (2008) 1536–1544.
[4] P. Edwards, A. O'Conner, M. Ramulu, Electron beam additive manufacturing of titanium components: properties and performance, J. Manuf. Sci. Eng. 135 (2013) 061016.
[5] Arcam, Arcam EBM A2 and S12: User's Manual, 2007.
[6] W.E. Frazier, Metal additive manufacturing: a review, J. Mater. Eng. Perform. 23 (2014) 1917–1928.
[7] S.S. Al-Bermani, M.L. Blackmore, W. Zhang, I. Todd, The origin of microstructural diversity, texture, and mechanical properties in electron beam melted Ti–6Al–4V, Metall. Mater. Trans. A 41 (2010) 3422–3434.
[8] L. Murr, E. Esquivel, S. Quinones, S. Gaytan, M. Lopez, E. Martinez, et al., Microstructures and mechanical properties of electron beam-rapid manufactured Ti–6Al–4V biomedical prototypes compared to wrought Ti–6Al–4V, Mater. Charact. 60 (2009) 96–105.
[9] K.S. Chan, M. Koike, R.L. Mason, T. Okabe, Fatigue life of titanium alloys fabricated by additive layer manufacturing techniques for dental implants, Metall. Mater. Trans. A 44 (2012) 1010–1022.
[10] M. Koike, P. Greer, K. Owen, G. Lilly, L.E. Murr, S.M. Gaytan, et al., Evaluation of titanium alloys fabricated using rapid prototyping technologies—electron beam melting and laser beam melting, Materials (Basel) 4 (2011) 1776–1792.
[11] A.A. Antonysamy, Microstructure, Texture and Mechanical Property Evolution During Additive Manufacture of Ti6Al4V Alloy Using Laser, Electron Beam, and Arc Melting Techniques for Aerospace Applications(PhD thesis) University of Manchester, 2012. (https://www.escholar.manchester.ac.uk/uk-ac-man-scw:160535).
[12] S.M. Gaytan, L.E. Murr, F. Medina, E. Martinez, M.I. Lopez, R.B. Wicker, Advanced metal powder based manufacturing of complex components by electron beam melting, Mater. Technol. 24 (2009) 180–190.
[13] N. Hrabe, T. Quinn, Effects of processing on microstructure and mechanical properties of a titanium alloy (Ti–6Al–4V) fabricated using electron beam melting (EBM), part 2: energy input, orientation, and location, Mater. Sci. Eng. A 573 (2013) 271–277.
[14] J. Karlsson, A. Snis, H. Engqvist, J. Lausmaa, Characterization and comparison of materials produced by Electron Beam Melting (EBM) of two different Ti–6Al–4V powder fractions, J. Mater. Process. Technol. 213 (2013) 2109–2118.
[15] K. Puebla, L. Murr, S. Gaytan, Effect of melt scan rate on microstructure and macrostructure for electron beam melting of Ti–6Al–4V, Mater. Sci. 2012 (2012) 259–264.
[16] L.E. Murr, S.M. Gaytan, A. Ceylan, E. Martinez, J.L. Martinez, Characterization of titanium aluminide alloy components fabricated by additive manufacturing using electron beam melting, Acta Mater. 58 (2010) 1887–1894.
[17] Z. Xu, W. Wen, T. Zhai, Effects of pore position in depth on stress/strain concentration and fatigue crack initiation, Metall. Mater. Trans. A 43 (2012) 2763–2770.
[18] N. Hrabe, T. Quinn, Effects of processing on microstructure and mechanical properties of a titanium alloy (Ti–6Al–4V) fabricated using electron beam melting (EBM), part 1: distance from build plate and part size, Mater. Sci. Eng. A 573 (2013) 264–270.
[19] A. Safdar, L.-Y. Wei, A. Snis, Z. Lai, Evaluation of microstructural development in electron beam melted Ti–6Al–4V, Mater. Charact. 65 (2012) 8–15.
[20] R. Morgan, A. Papworth, C. Sutcliffe, High density net shape components by direct laser re-melting of single-phase powders, J. Mater. Sci. 7 (2002) 3093–3100.
[21] M.N. Ahsan, A.J. Pinkerton, R.J. Moat, J. Shackleton, A comparative study of laser direct metal deposition characteristics using gas and plasma-atomized Ti–6Al–4V powders, Mater. Sci. Eng. A 528 (2011) 7648–7657.
[22] A. Bauereiß, T. Scharowsky, C. Körner, Defect generation and propagation mechanism during additive manufacturing by selective beam melting, J. Mater. Process. Technol. 214 (2014) 2522–2528.
[23] W.D. Pilkey, D.F. Pilkey, Peterson's Stress Concentration Factors, 3rd ed. John Wiley & Sons, Inc., Hoboken, New Jersey, 2008.
[24] L. Thijs, F. Verhaeghe, T. Craeghs, J. Van Humbeeck, J.-P. Kruth, A study of the microstructural evolution during selective laser melting of Ti–6Al–4V, Acta Mater. 58 (2010) 3303–3312.
[25] H. Attar, M. Calin, L.C. Zhang, S. Scudino, J. Eckert, Manufacture by selective laser melting and mechanical behavior of commercially pure titanium, Mater. Sci. Eng. A 593 (2014) 170–177.
[26] N. Otsu, Threshold Selection Method from Gray-Level Histograms, IEEE Trans Syst Man Cybern SMC-9 (1) (1979) 62–66.
[27] J.P. Kruth, M. Bartscher, S. Carmignato, R. Schmitt, L. De Chiffre, A. Weckenmann, Computed tomography for dimensional metrology, CIRP Ann. Manuf. Technol. 60 (2011) 821–842.
[28] S.R. Stock, Recent advances in X-ray microtomography applied to materials, Int. Mater. Rev. 53 (2008) 129–181.
[29] J.-P. Kruth, P. Mercelis, J. Van Vaerenbergh, L. Froyen, M. Rombouts, Binding mechanisms in selective laser sintering and selective laser melting, Rapid Prototyp. J. 11 (2005) 26–36.
[30] E. Maire, P.J. Withers, Quantitative X-ray tomography, Int. Mater. Rev. 59 (2013) 1–43.
[31] G. Ziółkowski, E. Chlebus, P. Szymczyk, J. Kurzac, Application of X-ray CT method for discontinuity and porosity detection in 316L stainless steel parts produced with SLM technology, Arch. Civ. Mech. Eng. (2014) 1–7.
[32] R.L. Higginson, C.M. Sellars, Worked Examples in Quantitative Metallography, Maney, London, 2003.
[33] R.S. Vitt, K. Ono, Hydrogen solubility in alpha titanium, Metall. Trans. 2 (1971) 608–609.
[34] E. Hernández-Nava, C.J. Smith, F. Derguti, S. Tammas-Williams, F. Léonard, P.J. Withers, et al., The effect of density and feature size on mechanical properties of isostructural metallic foams produced by additive manufacturing, Acta Mater. 85 (2015) 387–395.
[35] G.K.L. Ng, A.E.W. Jarfors, G. Bi, H.Y. Zheng, Porosity formation and gas bubble retention in laser metal deposition, Appl. Phys. A 97 (2009) 641–649.
[36] A.A. Antonysamy, J. Meyer, P.B. Prangnell, Effect of build geometry on the β-grain structure and texture in additive manufacture of Ti–6Al–4V by selective electron beam melting, Mater. Charact. 84 (2013) 153–168.

[37] S.S. Al-Bermani, An Investigation Into Microstructure and Microstructural Control of Additive Layer Manufactured Ti–6Al–4V by Electron Beam Melting(PhD thesis) University of Sheffield, 2010. (http://ethos.bl.uk/OrderDetails.do?uin=uk.bl.ethos.555712).
[38] P.A. Kobryn, E.H. Moore, S.L. Semiatin, The effect of laser power and traverse speed on microstructure, porosity, and build height in laser-deposited Ti–6Al–4V, Scr. Mater. 43 (2000) 299–305.
[39] H. Gong, K. Rafi, T. Starr, B. Stucker, The effects of processing parameters on defect regularity in Ti–6Al–4V parts fabricated by selective laser melting and electron beam melting, Solid Free. Fabr. Symp. (2013) 424–439.
[40] C. Qiu, N.J.E. Adkins, M.M. Attallah, Microstructure and tensile properties of selectively laser-melted and of HIPed laser-melted Ti–6Al–4V, Mater. Sci. Eng. A 578 (2013) 230–239.
[41] V. Juechter, T. Scharowsky, R.F. Singer, C. Körner, Processing window and evaporation phenomena for Ti–6Al–4V produced by selective electron beam melting, Acta Mater. 76 (2014) 252–258.